

## Deriving theoretical boundaries to address scale dependencies of triangle models for evapotranspiration estimation

Di Long,<sup>1,2</sup> Vijay P. Singh,<sup>1,3</sup> and Bridget R. Scanlon<sup>2</sup>

Received 28 October 2011; revised 9 January 2012; accepted 9 January 2012; published 7 March 2012.

[1] Satellite-based triangle models for evapotranspiration estimation are unique in interpreting the relationship between the normalized difference vegetation index (NDVI)/fractional vegetation cover ( $f_c$ ) and surface radiative temperature ( $T_{\text{rad}}$ ) across large heterogeneous areas. However, output and performance of triangle models may depend on the size of the domain being studied and resolution of the satellite images being used. The objective of this study was to assess domain and resolution dependencies of triangle models using progressively larger domains and Landsat Thematic Mapper/Enhanced Thematic Mapper Plus and Moderate Resolution Imaging Spectroradiometer sensors at the Soil Moisture-Atmosphere Coupling Experiment site in central Iowa on days of year 174 and 182 in 2002. Results show domain and resolution dependencies of the triangle models with large uncertainties in evaporative fraction (EF) estimates in terms of a mean absolute percentage difference (MAPD) up to  $\sim 50\%$ . A trapezoid model which requires derivation of theoretical limiting edges of the NDVI- $T_{\text{rad}}$  space is proposed to constrain domain and resolution dependencies of triangle models. The theoretical warm edge can be derived by solving for temperatures of the driest bare surface and the fully vegetated surface with the largest water stress implicit in both radiation budget and energy balance equations. Areal average air temperature can be taken as the theoretical cold edge. The triangle model appears to perform well across large areas ( $\sim 10^4 \text{ km}^2$ ) but fails to predict EF over small areas ( $\sim 10^2 \text{ km}^2$ ). The trapezoid model can effectively reduce domain and resolution dependencies and constrain errors of the EF estimates with an MAPD of  $\sim 10\%$ .

**Citation:** Long, D., V. P. Singh, and B. R. Scanlon (2012), Deriving theoretical boundaries to address scale dependencies of triangle models for evapotranspiration estimation, *J. Geophys. Res.*, 117, D05113, doi:10.1029/2011JD017079.

### 1. Introduction

[2] Numerous hydrology, water resources, agriculture, and forestry related studies and applications require quantification of evapotranspiration (ET) across a range of spatial and temporal scales [Anderson *et al.*, 2007; Long *et al.*, 2011; McCabe and Wood, 2006]. Satellite remote sensing provides an unprecedented opportunity to derive surface and atmospheric variables over large areas, which are unattainable from ground-based measurements (e.g., weighing lysimeter, Energy Balance Bowen Ratio (EBBR) systems, and eddy covariance (EC) systems) and meaningful in ET modeling over large heterogeneous areas. In this context, a number of satellite-based land surface flux models have emerged since the 1980s by incorporating remotely sensed

variables and routinely observed meteorological data [Kalma *et al.*, 2008]. Among these models, the triangle model is unique in interpreting the relationship between the Normalized Difference Vegetation Index (NDVI)/fractional vegetation cover ( $f_c$ ) and surface radiative temperature ( $T_{\text{rad}}$ ) to deduce evaporative fraction (EF, ratio of latent heat flux (LE) to available energy ( $R_n - G$ )) over large areas [Carlson *et al.*, 1994; Gillies and Carlson, 1995; Jiang and Islam, 2001; Price, 1990; Sandholt *et al.*, 2002]. This type of model has advantages in utilizing information from visible, near-infrared, and thermal infrared bands to deduce EF without largely depending on ground observations.

[3] There are, however, several common issues associated with triangle models that have not been adequately addressed. First, triangle models have consistently underestimated [e.g., Choi *et al.*, 2009; Jiang and Islam, 2003; Wang *et al.*, 2006] or overestimated EF/ET [e.g., Batra *et al.*, 2006; Jiang and Islam, 2003; Jiang *et al.*, 2009] compared with ground-based measurements. However, reasons for these deviations have not been fully investigated or appropriately interpreted from a standpoint of model physics and scale effect. Second, most triangle models are combined with moderate- or low-spatial-resolution satellite sensors; that is,

<sup>1</sup>Department of Biological and Agricultural Engineering, Texas A&M University, College Station, Texas, USA.

<sup>2</sup>Bureau of Economic Geology, Jackson School of Geosciences, University of Texas at Austin, Austin, Texas, USA.

<sup>3</sup>Department of Civil and Environmental Engineering, Texas A&M University, College Station, Texas, USA.

the National Oceanic and Atmospheric Administration-Advanced Very High Resolution Radiometer (NOAA-AVHRR) [Batra *et al.*, 2006; Jiang and Islam, 2001; Sandholt *et al.*, 2002], Moderate Resolution Imaging Spectroradiometer (MODIS) [Tang *et al.*, 2010; Wang *et al.*, 2006], and Meteosat Second Generation satellite (MSG)-Spinning Enhanced Visible and Infrared Imager (SEVIRI) [Stisen *et al.*, 2008], for estimating EF over large areas. However, triangle models are rarely applied with high-spatial-resolution images; for example, Landsat Thematic Mapper (TM)/Enhanced Thematic Mapper Plus (ETM<sup>+</sup>). Determining effective techniques to use data from various sensors has been the focus of considerable research [McCabe and Wood, 2006].

[4] Third, a recurring issue for application of derived satellite data is whether techniques for one scale are appropriate to another [Carlson *et al.*, 1995]. Methods of addressing spatial and temporal disparities between landscape heterogeneity and sensor and model resolution seem to be limited, because an adequately developed theory of scale dependence or scaling in hydrology does not yet exist [Beven and Fisher, 1996]. Particularly in surface flux estimation, little work has been performed to investigate differences in model outputs between using easily obtained moderate- or low-spatial-resolution sensors and relatively infrequent high-spatial-resolution sensors. These issues remain unresolved and affect surface flux estimation in the operational ET estimation and hydrological communities [McCabe and Wood, 2006].

[5] Fourth, there is another significant scale issue intrinsic in triangle models: domain scale effect. It is referred to as the dependence of model outputs on the size of the domain where the model is applied or on the size of the usable image [Long *et al.*, 2011]. There are two limiting edges constituting envelopes of the NDVI/ $f_c$ - $T_{\text{rad}}$  space in triangle models. They play a paramount role in determining the magnitude of EF. The upper envelope (here the  $x$  axis represents NDVI or  $f_c$  and the  $y$  axis represents  $T_{\text{rad}}$ ) is referred to as the warm edge, pixels on which are taken as surfaces with the largest water stress for a range of NDVI/ $f_c$ . In contrast, the lower envelope is called the cold edge, pixels on which represent surfaces without water stress; that is, evaporating and transpiring at potential rates. EF for a pixel at a specific NDVI/ $f_c$  interval is deduced by weighting the extreme  $T_{\text{rad}}$  values within the interval in terms of the  $T_{\text{rad}}$  of the pixel. To that end, the warm and cold edges are essential to configuring the triangle space by providing important boundary conditions of the contextual NDVI/ $f_c$ - $T_{\text{rad}}$  relationship and subsequently to determining EF for pixels within these limiting edges. Normally, one focuses primarily on a single size of the domain of interest; for example, the Soil Moisture-Atmosphere Coupling Experiment (SMACEX) site of  $\sim 670 \text{ km}^2$  in central Iowa [Choi *et al.*, 2009], the Heihe River basin  $\sim 38,000 \text{ km}^2$  in northwestern China [Tang *et al.*, 2010], and the Southern Great Plains site of  $\sim 140,000 \text{ km}^2$  [Batra *et al.*, 2006; Wang *et al.*, 2006]. Areas beyond a study site are rarely taken into account. Nevertheless, determination of warm and cold edges of the NDVI/ $f_c$ - $T_{\text{rad}}$  space may depend on the size of the domain being studied. Alternatively, thermal band(s) of a variety of satellite sensors have varying capacity to discriminate the thermal properties of the land surface and therefore to derive  $T_{\text{rad}}$ . In other words,

resolution of  $T_{\text{rad}}$  retrievals may also influence the definition and determination of limiting edges: The resolution dependence implies that varying spatial resolutions of satellite images are likely to generate varying EF for a given study site.

[6] A multitude of significant studies on examining resolution scale effects of satellite-based ET modeling has been performed to improve our understanding of the spatial scaling behavior of ET and its relation to controlling factors on the land surface. Carlson *et al.* [1995] investigated resolution dependence of triangle models by linearly aggregating  $T_{\text{rad}}$  of high spatial resolution derived from the NS001 multispectral scanner (5 m) to mimic low-spatial-resolution data, with resolutions of 20, 80, and 320 m. They observed successive movement of the warm edge toward the cold edge with increasing pixel size, but concluded that the objectively determined warm edge coincided with the domain of soil moisture availability isopleths and therefore the triangle with its warm edge was not substantially changed. Gillies *et al.* [1997] indicated that scale issues may influence ET retrievals from triangle models because low-resolution data would not be able to define limiting edges [Gillies and Carlson, 1995]. Batra *et al.* [2006] and Venturini *et al.* [2004] showed that the NDVI- $T_{\text{rad}}$  space and EF estimates were similar for triangle models applied to MODIS and AVHRR sensors. Brunzell *et al.* [2008] examined scaling behavior of ET from a triangle model at different resolutions (e.g., 1 km, 2 km, 4 km, and 8 km) using wavelet multiresolution analysis combined with low-pass filters and entropy theory. A similar study was performed using a range of satellite sensors (i.e., Landsat, MODIS, and Geostationary Operational Environmental Satellites (GOES)) to quantify which spatial scales are dominant in determining the ET flux [Brunzell and Anderson, 2011]. Deviated from the previous studies, this study focuses primarily on domain scale effects and resolution scale effects in EF estimation by triangle models from a perspective of model physics.

[7] The objectives of this study were to (1) evaluate reasons for overestimation and underestimation of EF by triangle models from a standpoint of model physics; (2) examine utility of triangle models using high-spatial-resolution satellite imagery; (3) explore domain and resolution dependencies of triangle models; and (4) develop a framework to constrain those dependencies for EF estimation. Section 2 introduces fundamentals of triangle models and development of a trapezoid model to address the scale dependencies, followed by a description of study site, data collection, and variable derivation in section 3. Sections 4 and 5 provide a systematic analysis of the domain dependence and resolution dependence of triangle models, respectively. Major findings of this study are given in section 6.

## 2. Methodology

### 2.1. Fundamentals of Triangle Models

#### 2.1.1. Original Form of Triangle Models

[8] There is a series of triangle models [e.g., Batra *et al.*, 2006; Jiang and Islam, 1999; Moran *et al.*, 1994; Sandholt *et al.*, 2002] developed which share a similarity in interpreting the relationship between NDVI/ $f_c$  and  $T_{\text{rad}}$ . In

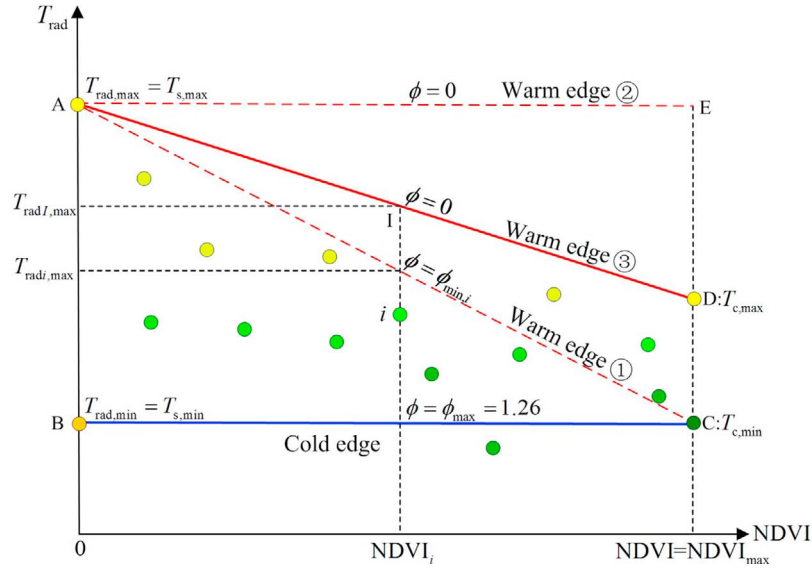


**Figure 1.** Scatterplot of remotely sensed NDVI and  $T_{\text{rad}}$ . Colored circles represent pixels with varying NDVI and  $T_{\text{rad}}$ . Trapezoid ABCD represents theoretical limits of the NDVI- $T_{\text{rad}}$  space. Point A represents the driest bare surface (i.e.,  $EF = 0$ ), point B represents the wettest bare surface without water stress (i.e.,  $EF = 1$ ), point C represents the fully vegetated surface without water stress (i.e.,  $EF = 1$ ), and point D represents the fully vegetated surface with the largest stress (i.e.,  $EF = 0$ ). Side AC is warm edge 1 of triangle ABC, whose  $\phi$  values are equal to  $\phi_{\text{min},i}$  for each NDVI value or NDVI class  $i$ . Side AE is warm edge 2 of rectangle models (simplified from triangle models) whose  $\phi$  value is equal to zero. Side AD is warm edge 3 representing surfaces of  $EF = 0$  for a full range of NDVI in the trapezoidal model. Side BC is the horizontal cold edge representing surfaces of  $EF = 1$  for a full range of NDVI.

general, envelopes of the  $\text{NDVI}/f_c$ - $T_{\text{rad}}$  space constitute a trapezoid (or a cucumber-like shape), which is conceptually and/or technically simplified as a triangle or even a rectangle shown in section 2.1.2. In this study, the terminology of triangle models include conceptually and/or technically simplified triangles and trapezoid models appearing in the literature which entail derivation of warm and/or cold edges directly from the scatterplot of  $\text{NDVI}/f_c$  and  $T_{\text{rad}}$  for a certain size of satellite images. The major differences in these models lie in triangular or trapezoidal configuration of the space. Figure 1 illustrates the contextual space and several types of limiting edges for triangle models.

[9] The triangle model (triangle ABC in Figure 1) developed by *Jiang and Islam* [1999, 2001] makes use of parameter  $\phi$  derived from the NDVI- $T_{\text{rad}}$  space to partition net energy and then estimates latent heat flux on the basis of the Priestley-Taylor equation:

$$\text{LE} = \phi \left( \frac{\Delta}{\Delta + \gamma} \right) (R_n - G) \quad (1)$$

where  $\Delta$  is the slope of saturation vapor pressure-temperature relationship at air temperature ( $T_a$ ) ( $\text{kPa}^\circ\text{C}^{-1}$ );  $\gamma$  is the psychrometric constant ( $\text{kPa}^\circ\text{C}^{-1}$ );  $R_n$  is the net radiation ( $\text{W m}^{-2}$ ); and  $G$  is the soil heat flux ( $\text{W m}^{-2}$ ). Parameter  $\phi$  integrates effects of soil moisture availability, vapor pressure gradient, and aerodynamic and surface resistances on  $EF$ , which is expressed as

$$\phi = \frac{T_{\text{radi,max}} - T_{\text{radi}}}{T_{\text{radi,max}} - T_{\text{radi,min}}} (\phi_{\text{max},i} - \phi_{\text{min},i}) + \phi_{\text{min},i} \quad (2)$$

where  $T_{\text{radi,max}}$  and  $T_{\text{radi,min}}$  are the maximum and minimum  $T_{\text{rad}}$  values for NDVI class  $i$ ; and  $T_{\text{radi}}$  is the  $T_{\text{rad}}$  value of a pixel in NDVI class  $i$ ;  $\phi_{\text{max},i}$  is the maximum value of parameter  $\phi$  ( $=$  Priestley-Taylor parameter of 1.26); that is, the parameter  $\phi$  of cold edge BC is equal to 1.26;  $\phi_{\text{min},i}$  is the minimum value of parameter  $\phi$  for NDVI class  $i$ , which is the parameter  $\phi$  of the warm edge AC. Parameter  $\phi_{\text{min},i}$  is assumed to be proportional to  $\text{NDVI}/f_c$  [*Jiang and Islam*, 1999, 2001]; that is,  $\phi_{\text{min},i} = 1.26 \cdot \text{NDVI}_i / \text{NDVI}_{\text{max}}$  where  $\text{NDVI}_{\text{max}}$  is the maximum value of NDVI across a scene. In terms of the assumption, parameter  $\phi_{\text{min},i}$  is equal to 0 at  $\text{NDVI} = 0$  which is assumed to represent the driest bare surface and is equal to 1.26 at  $\text{NDVI} = \text{NDVI}_{\text{max}}$ ; that is, the point of intersection of side AC and side BC. *Stisen et al.* [2008] modified the linear correlation of  $\phi_{\text{min},i}$  with NDVI as a power function with an exponent of 2 within the triangle model. As such,  $\phi_{\text{min},i}$  is nonlinearly correlated with NDVI, which attempts to account for a more rapid change of  $\phi_{\text{min},i}$  for high NDVI values than those for low NDVI values along with the warm edge. Note that variations in  $T_{\text{rad}}$  in the triangular configuration of the  $\text{NDVI}/f_c$ - $T_{\text{rad}}$  space are due primarily to variations in soil moisture and  $f_c$ , instead of variations in temperatures of vegetation canopies [*Carlson*, 2007].

[10] In the computation,  $T_{\text{radi,max}}$  and  $T_{\text{radi,min}}$  are derived from warm and cold edges of the  $\text{NDVI}/f_c$ - $T_{\text{rad}}$  space, respectively, which are a function of  $\text{NDVI}/f_c$ . Therefore, the value of parameter  $\phi$  for a pixel can be uniquely determined by its  $T_{\text{rad}}$  and  $\text{NDVI}/f_c$  values on the basis of equation (2).

Combining equations (1) and (2), EF for a pixel can therefore be written as

$$EF = \left[ \frac{T_{\text{rad},i,\text{max}} - T_{\text{rad},i}}{T_{\text{rad},i,\text{max}} - T_{\text{rad},i,\text{min}}} (\phi_{\text{max},i} - \phi_{\text{min},i}) + \phi_{\text{min},i} \right] \cdot \left( \frac{\Delta}{\Delta + \gamma} \right) \quad (3)$$

In equation (3) the quantity  $\Delta/(\Delta+\gamma)$  varies slightly with  $T_a$ ; therefore, EF is largely determined by  $T_{\text{rad},i,\text{max}}$  and  $T_{\text{rad},i,\text{min}}$  for a given  $T_{\text{rad},i}$  value in NDVI/ $f_c$  class  $i$ . It is particularly important to note that in reality, a cluster of data points between NDVI/ $f_c$  and  $T_{\text{rad}}$  rarely constitute a triangle. This means that warm edge AC cannot intersect with cold edge BC within reasonable ranges of  $\text{NDVI} \leq \text{NDVI}_{\text{max}}$  or  $f_c \leq f_{c,\text{max}} = 1$ . As such, the boundaries of triangle models often technically constitute a trapezoidal shape [e.g., *Choi et al.*, 2009; *Jiang et al.*, 2009; *Venturini et al.*, 2004; *Wang et al.*, 2006]. In some cases,  $\phi_{\text{min},i}$  values in equation (3) of the observed warm edge are simplified as zero, justified by the effects of root zone water stress on vegetated surfaces for a full range of NDVI/ $f_c$  [*Choi et al.*, 2009; *Kalma et al.*, 2008].

[11] The warm and/or cold edges of triangle models are derived from the remotely sensed NDVI/ $f_c$ - $T_{\text{rad}}$  scatterplot by linear fit to data pairs of the maximum (the warm edge)/minimum (the cold edge)  $T_{\text{rad}}$  values and the corresponding NDVI/ $f_c$  values at each NDVI/ $f_c$  class interval [e.g., *Choi et al.*, 2009; *Nemani et al.*, 1993; *Sandholt et al.*, 2002]. It is noted that the triangle models developed by *Jiang and Islam* [1999, 2001, 2003] do not explicitly show how warm and cold edges of  $T_{\text{rad}}$  are derived; these published studies only show how extreme  $\phi$  values (i.e.,  $\phi_{\text{min}}$  at NDVI/ $f_c = 0$ ,  $\phi_{\text{min}}$  at NDVI = NDVI<sub>max</sub> or  $f_c = 1$ , and  $\phi_{\text{max}}$ ) of conceptually existing warm and cold edges are specified so as to extrapolate  $\phi$  values for pixels in all NDVI/ $f_c$  classes.

### 2.1.2. Simplification of Triangle Models: Rectangle Models

[12] *Batra et al.* [2006] and *Jiang et al.* [2009] simplified parameter  $\phi$  in equation (2) as

$$\phi = \frac{T_{\text{rad},\text{max}} - T_{\text{rad}}}{T_{\text{rad},\text{max}} - T_{\text{rad},\text{min}}} \phi_{\text{max}} \quad (4)$$

where  $T_{\text{rad},\text{max}}$  and  $T_{\text{rad},\text{min}}$  are the maximum and minimum  $T_{\text{rad}}$  throughout an entire scene. Unlike  $T_{\text{rad},i,\text{max}}$  and  $T_{\text{rad},i,\text{min}}$  which vary with NDVI/ $f_c$  in equation (3),  $T_{\text{rad},\text{max}}$  and  $T_{\text{rad},\text{min}}$  in equation (4) remain constant across a scene and therefore constitute two horizontal limiting edges (i.e., side AE and BC in Figure 1). It is apparent from equation (4) that parameter  $\phi$  of the warm edge (i.e.,  $\phi_{\text{min},i}$  in equation (3)) is simplified as zero. The triangle ABC is indeed simplified as a rectangle ABCE. Warm edge AE theoretically corresponds to the driest surfaces for a full range of NDVI/ $f_c$  with EF = 0.

[13]  $T_{\text{rad},\text{max}}$  is deduced by extrapolating the warm edge from regression analysis to intersect with NDVI = 0, which is assumed to be the highest temperature over the bare soil [*Batra et al.*, 2006; *Jiang et al.*, 2009], and  $T_{\text{rad},\text{min}}$  is determined by the  $T_{\text{rad}}$  of the pixel with the largest NDVI value [*Jiang and Islam*, 2001]. Area average  $T_a$  [*Jiang and Islam*, 2003], average inland water surface temperature [*Batra et al.*, 2006; *Jiang et al.*, 2009], or the temperature

from extrapolating the warm edge to intersect with  $f_c = 1$  [*Tang et al.*, 2010] was also taken as the cold edge. Consequently,  $\phi$  values for the remaining pixels between the limiting edges can be determined only by their  $T_{\text{rad}}$  values using equation (4). EF from the rectangle models can therefore be calculated as

$$EF = \frac{T_{\text{rad},\text{max}} - T_{\text{rad}}}{T_{\text{rad},\text{max}} - T_{\text{rad},\text{min}}} \phi_{\text{max}} \cdot \left( \frac{\Delta}{\Delta + \gamma} \right) \quad (5)$$

In this study, scale dependencies of the triangle model of the original form (equation (3)) were investigated, in which both warm and cold edges were derived by regression analysis, as other treatments for deriving the cold edge (e.g., extrapolating the warm edge to intersect with NDVI = NDVI<sub>max</sub> or  $f_c = 1$ ) resulted in a large number of data points being left out of these envelopes.

## 2.2. Derivation of Theoretical Limiting Edges for a Trapezoid Model

### 2.2.1. Observed Limiting Edges Versus Theoretical Limiting Edges

[14] Limiting edges involved in both the traditional triangle model in equation (3) and the simplified rectangle model in equation (5) are derived from the scatterplots of the NDVI- $T_{\text{rad}}$  space. They are referred to as the observed limiting edges in this study. These approaches are only valid when both minimum and maximum LE can be observed within the boundaries of the study area [*Choi et al.*, 2009; *Kalma et al.*, 2008; *Stisen et al.*, 2008]. One important assumption is that the major differences in EF estimates are not introduced by atmospheric conditions and surface characteristics (e.g., wind velocity and vegetation height), but mainly contributed by variation in soil moisture availability. This assumption necessitates a large or heterogeneous study area with a broad range of soil wetness conditions and relatively uniform atmospheric forcing. Another assumption involved is that the use of triangle models does not allow the presence of water stressed full cover vegetation since the triangle models create a singularity at point C. Vegetation with a range of  $f_c$  transpires at near-potential rates regardless of surface soil water content; the triangle models do not account for water stress on vegetation [*Carlson*, 2007].

### 2.2.2. Theoretical Limiting Edges

[15] We suggest that theoretical boundaries (real physical limits) of EF (i.e., EF = 0 and EF = 1) for a range of  $f_c$ , objectively exist within a given study site under certain meteorological conditions. The remotely sensed  $f_c$ - $T_{\text{rad}}$  space may not be able to detect extreme wet/dry conditions of EF for a full range of  $f_c$  in semiarid/arid environments or humid environments [*Stisen et al.*, 2008] owing to the absence of these extreme surfaces and/or the spatially integrated nature of satellite observations [*Long et al.*, 2011; *Stisen et al.*, 2008]. These observed limiting edges may be varied owing to the variation in the domain size being studied or the satellite image being used. Differing resolutions of satellite images and domain sizes would result in ambiguity and uncertainty in derivation of limiting edges and therefore the resulting EF estimates. The use of the theoretical boundaries could provide a deterministic solution of EF and soil moisture across a scene.

[16] The theoretical boundaries where the upper limit of EF is 0 and the lower limit of EF is 1 of the NDVI- $T_{\text{rad}}$  space are assumed to constitute a trapezoid (i.e., trapezoid ABCD in Figure 1), rather than a triangle (i.e., triangle ABC) or a rectangle (rectangle ABCE). In other words, the theoretical warm edge (warm edge 3), on which parameter  $\phi$  and EF are equal to zero, is above the hypotenuse of the triangle ABC (warm edge 1). This is because the temperature of the fully vegetated surface with the largest water stress and showing complete stomatal closure (point D) is higher than that of the fully vegetated surface without water stress (point C) [Moran *et al.*, 1994]. However, the temperature of the fully vegetated surface with the largest water stress (point D) is lower than that of the bare surface with the largest water stress (point A) as sunlit vegetation is generally cooler than sunlit bare soil [Carlson, 2007]. As such, the theoretical warm edge should be lower than that of rectangle ABCE (warm edge 2).

[17]  $\phi_{\text{min},i}$  in triangle models is assumed to be correlated only with NDVI [Jiang and Islam, 2001; Stisen *et al.*, 2008], with the largest value ( $= 1.26$ ) on the fully vegetated surface without water stress and the smallest value ( $= 0$ ) on the driest bare surface. The assumed linear/nonlinear correlation between  $\phi_{\text{min},i}$  and NDVI may be true for the two extremes; however, it may not be the case for the whole range of NDVI/ $f_c$  owing to a more complex unknown relationship between  $\phi_{\text{min},i}$  and other factors.

[18] The theoretical limiting edges would rarely occur in an image scene; however, the use of the theoretical boundaries of the NDVI- $T_{\text{rad}}$  space would provide the metrics to confine EF for all pixels and be useful in reducing uncertainties associated with use of observed limiting edges and determination of  $\phi_{\text{min}}$  values for a full range of NDVI/ $f_c$  owing to the domain and resolution dependencies.

### 2.2.3. Determination of Theoretical Limiting Edges

[19] Moran *et al.* [1994] provided an approach for calculating theoretical temperatures for dry bare soil (point A), saturated bare soil (point B), full-cover, well-watered vegetation (point C), and full-cover vegetation with no available water (point D). This approach, however, requires precise on-site measurements of radiation, vapor pressure deficit, and air temperature for the four representative surfaces within a study site [Stisen *et al.*, 2008], which means that it requires relatively more priori knowledge and may reduce robustness of the model. McVicar and Jupp [2002] provided the Normalized Difference Temperature Index (NDTI) approach which calculates extreme temperatures at meteorological stations by inverting a Resistance Energy Balance Model (REBM). Here, we derive theoretical temperatures for point A and point D ( $T_{\text{s,max}}$  and  $T_{\text{c,max}}$ ) from radiation budget and energy balance equations, because these temperatures are both involved in the longwave radiation component in the radiation budget equation and the temperature gradient of the sensible heat flux component in the energy balance equation. In this manner, vapor pressure deficit is no longer explicitly involved in the calculation. For point A, the radiation budget and energy balance equations can be shown as

$$\begin{aligned} R_{\text{n,s}} &= (1 - \alpha_s)S_d + \varepsilon_s L_d - L_u \\ &= (1 - \alpha_s)S_d + \varepsilon_s \varepsilon_a \sigma T_a^4 - \varepsilon_s \sigma T_s^4 \end{aligned} \quad (6)$$

$$R_{\text{n,s}} - G = H_s + \text{LE}_s = \rho c_p \left( \frac{T_s - T_a}{r_{\text{a,s}}} \right) + \text{LE}_s \quad (7)$$

where  $R_{\text{n,s}}$  is the net radiation for the bare surface ( $\text{W m}^{-2}$ );  $\alpha_s$  is the bare surface albedo;  $S_d$  is the incoming shortwave radiation ( $\text{W m}^{-2}$ );  $\varepsilon_s$  is the bare surface emissivity (e.g., 0.95) [Tasumi, 2003];  $\varepsilon_a$  is the atmospheric emissivity, which is a function of  $T_a$  (K) and vapor pressure  $e_a$  (hPa) [Brutsaert, 1975];  $L_d$  and  $L_u$  are the incoming and outgoing longwave radiation ( $\text{W m}^{-2}$ ), respectively;  $\sigma$  is the Stefan-Boltzmann constant ( $5.67 \times 10^{-8} \text{ W m}^{-2} \text{ K}^{-4}$ );  $T_s$  is the bare surface temperature (K);  $G$  is the soil heat flux ( $\text{W m}^{-2}$ ),  $H_s$  and  $\text{LE}_s$  are the sensible and latent heat fluxes ( $\text{W m}^{-2}$ ) of the bare surface, respectively;  $\rho$  is the air density ( $\text{kg m}^{-3}$ );  $c_p$  is the specific heat of air at constant pressure ( $\text{J kg}^{-1} \text{ K}^{-1}$ ), and  $r_{\text{a,s}}$  is the resistance for the bare surface ( $\text{s m}^{-1}$ ). Here,  $r_{\text{a,s}}$  is computed with Kondo's [1994] formulas which combines the aerodynamic resistance with the surface resistance. Atmospheric stability corrections in  $r_{\text{a,s}}$  need to be performed. The first two terms of Taylor's formula of  $L_u$  at  $T_a$  can be written as [Nishida *et al.*, 2003b]

$$L_u = \varepsilon_s \sigma T_s^4 \approx \varepsilon_s \sigma T_a^4 + 4\varepsilon_s \sigma T_a^3 (T_s - T_a) \quad (8)$$

Substituting equation (8) into equation (6) results in

$$R_{\text{n,s}} = (1 - \alpha_s)S_d + \varepsilon_s \varepsilon_a \sigma T_a^4 - \varepsilon_s \sigma T_a^4 - 4\varepsilon_s \sigma T_a^3 (T_s - T_a) \quad (9)$$

Let the first three terms on the right of equation (9) be  $R_{\text{n,s0}}$ , which is the net radiation for the bare surface in which  $T_s$  is approximated by  $T_a$  in the component of  $L_u$ . Combining  $R_{\text{n,s0}}$ , equations (7) and (9), and let  $G = cR_{\text{n,s}}$  where  $c$  is a calibrated proportionality coefficient (0.35 for the bare surface), one obtains

$$T_s = \frac{R_{\text{n,s0}} - \text{LE}_s / (1 - c)}{4\varepsilon_s \sigma T_a^3 + \rho c_p / [r_{\text{a,s}}(1 - c)]} + T_a \quad (10)$$

For the driest bare surface,  $\text{LE}_s$  is assumed to be zero. Therefore, the surface temperature for point A in trapezoid ABCD,  $T_{\text{s,max}}$ , is

$$T_{\text{s,max}} = \frac{R_{\text{n,s0}}}{4\varepsilon_s \sigma T_a^3 + \rho c_p / [r_{\text{a,s}}(1 - c)]} + T_a \quad (11)$$

$r_{\text{a,s}}$  is also a function of  $T_{\text{s,max}}$  involved in the Monin-Obukhov length for stability correction. Therefore, equation (11) needs to be solved in an iterative manner. Derivation of  $T_{\text{s,max}}$  requires generally steady atmospheric conditions ( $T_a$  and  $u_*$ ) for a study site.

[20] In a similar manner, we derived the temperature for the fully vegetated surface (point D) with the largest water stress,  $T_{\text{c,max}}$ :

$$T_{\text{c,max}} = \frac{R_{\text{n,c0}}}{4\varepsilon_c \sigma T_a^3 + \rho c_p / r_{\text{a,c}}} + T_a \quad (12)$$

where  $R_{\text{n,c0}}$  is the radiation for the fully vegetated surface in which vegetation canopy temperature,  $T_c$ , is approximated by  $T_a$  in the component of  $L_u$ ;  $\varepsilon_c$  is the vegetation emissivity (0.98) [Tasumi, 2003]; and  $r_{\text{a,c}}$  is the aerodynamic resistance for the fully vegetated surface. The surface is assumed to be

covered by dense vegetation with a vegetation height  $h_c$  of 1 m. Therefore, physiologic parameters for the surface (i.e., zero displacement  $d$ , roughness length for momentum transfer  $z_{om}$ , and roughness length for heat transfer  $z_{oh}$ ) can be specified as  $d = 2/3 h_c$ ,  $z_{om} = 0.1 h_c$ , and  $z_{oh} = z_{om}/7$ , respectively [Garratt and Hicks, 1973]. At point D, the canopy resistance becomes extremely large (e.g., 1000–1500  $s m^{-1}$ ) owing to the nearly complete stomatal closure under the largest water stress of the soil surface and root zone [Moran *et al.*, 1994]. As such,  $r_{a,c}$  plays a more important role in determining the temperature difference between  $T_{c,max}$  and  $T_a$ . Detailed descriptions about derivation of  $T_{s,max}$  and  $T_{c,max}$  can be found in the work of Long and Singh [2012]. Note that in equation (12),  $G$  for the fully vegetated surface is taken as zero.

[21] Surface albedo of points A and D ( $\alpha_s$  in  $R_{n,s0}$  and  $\alpha_c$  in  $R_{n,c0}$ ) can be obtained from measurements or deduced by extending the upper envelope of the NDVI- $\alpha$  space to NDVI = 0 and NDVI = NDVI<sub>max</sub>, respectively. Areal average air temperature could be taken as the lower theoretical limiting edge (i.e.,  $T_{s,min} = T_{c,min} = T_a$ ), given that the temperature gradients over these saturated surfaces would approach zero. This may not be able to deal with conditions of extremely high vapor pressure deficit (e.g., >3 kPa) or advection. However, it is an operational way to determine the theoretical lower limiting edge and obviates the requirement of vapor pressure deficit in the work of Moran *et al.* [1994]. The use of  $T_{rad}$  for fully vegetated surface would be an alternative to determine the cold edge of the NDVI/ $f_c$ - $T_{rad}$  space.

[22] After the theoretical limiting edges are determined by the above procedures, EF can be derived as

$$EF = \phi_{max} \frac{T_{rad,max} - T_{radi}}{T_{rad,max} - T_{rad,min}} \cdot \frac{\Delta}{\Delta + \gamma} \quad (13)$$

where  $T_{rad,max}$  and  $T_{rad,min}$  are the temperatures of the theoretical limiting edges (see Figure 1) for pixel  $i$ .

### 3. Study Site and Data Descriptions

#### 3.1. Study Site

[23] The Soil Moisture-Atmosphere Coupling Experiment (SMACEX) campaign, conducted in central Iowa, ranging in latitude between 41.87°N and 42.05°N and in longitude between -93.83°W and -93.39°W (Figure 2) during the period from 15 June (DOY 166) through 8 July (DOY 189) in 2002, provides extensive measurements of soil, vegetation, and meteorological properties and states to provide a greater understanding of mechanisms of water and heat exchanges with the atmosphere [Kustas *et al.*, 2005]. Data from SMACEX provide a unique opportunity to perform rigorous validation and comparison of a series of satellite-based models for surface flux estimation. The field campaign was primarily conducted in the Walnut Creek watershed, just south of Ames in central Iowa. Rain-fed corn and soybean fields dominate the Walnut Creek watershed. During the course of campaign, crops and vegetation grew rapidly. The surface soil moisture changed from dry to wet after rainfall events in early July.

[24] The mean annual rainfall of this region is 835 mm, which is classified as a humid climate. Precipitation during

the SMACEX campaign occurred a few days prior to 15 June (DOY 166), with a minor rainfall event of 0–5 mm on 20 June (DOY 171). This was followed by a rain-free period for the Walnut Creek watershed until 4 July (DOY 185). DOY 189 showed relatively wet surface conditions. In a typical growing season, the most rapid growth in corn and soybean crops is observed in June and July. The topography is characterized by low relief and poor surface drainage.

#### 3.2. Flux Tower Measurements

[25] A network consisting of 12 fully operational meteorological flux (METFLUX) towers was deployed within or in the vicinity of the Walnut Creek watershed (FT03, 06, 23, 24, 25, and 33 were outside the watershed), employing EC systems at 12 field sites, in which 6 sites were corn and 6 sites were soybean. These towers were instrumented with a variety of sensors for measuring turbulent fluxes of latent and sensible heat, as well as radiation components (i.e., incoming and outgoing shortwave and longwave radiation) and soil heat fluxes at 30 min intervals. Additional in situ hydrometeorological observations encompassed 10 min averaged temperature, relative humidity, and wind speed and direction. Observed fluxes for two image acquisition dates were used to evaluate the triangle model and the trapezoid model. Details of these sensors and processing of measurements can be found in the work of Kustas *et al.* [2005] and Prueger *et al.* [2005].

#### 3.3. Remote Sensing Data Sources and Variable Derivation

[26] The period of SMACEX permitted three scenes of cloud-free Landsat TM/ETM<sup>+</sup> imagery, two of which were used in this study. One scene of Landsat TM was acquired at 10:20 local time on DOY 174 spanning vegetated canopy cover from 50% to 75%. The other scene of Landsat ETM<sup>+</sup> acquired at 10:42 local time on DOY 182 spanning vegetated canopy cover from 75% to 90%.  $T_{rad}$  was derived from the thermal band of the Landsat imagery using the method proposed by Li *et al.* [2004] specifically for the SMACEX site. Albedo was retrieved from the visible and near-infrared bands of the Landsat imagery using Allen *et al.*'s [2007] algorithm. MODIS based  $T_{rad}$  products (MOD11\_L2) covering the entire scene of the Landsat ETM<sup>+</sup> imagery acquired at 11:00 local time on DOY 182, and MODIS 16 day NDVI composite products (MOD13A2 on DOY 177) were jointly used in investigating the resolution dependence of the triangle model.

### 4. Domain Dependence of the Triangle Model

#### 4.1. Four Domains and Three Scenarios of Limiting Edges

[27] Domain dependence of the triangle model was systematically examined by applying it to variable domains covering the SMACEX site within the coverage of Landsat TM/ETM<sup>+</sup> imagery (a swath of 185 km) for days of year 174 and 182. The boundary of the SMACEX site is a rectangle with an aspect ratio of 2:1 (domain 1 shown in Figure 3). Domains 2 and 3 are progressively larger domains with length and width equal to two and four times those of domain 1. Domain 4 is the entire coverage of the acquired Landsat ETM<sup>+</sup> imagery.

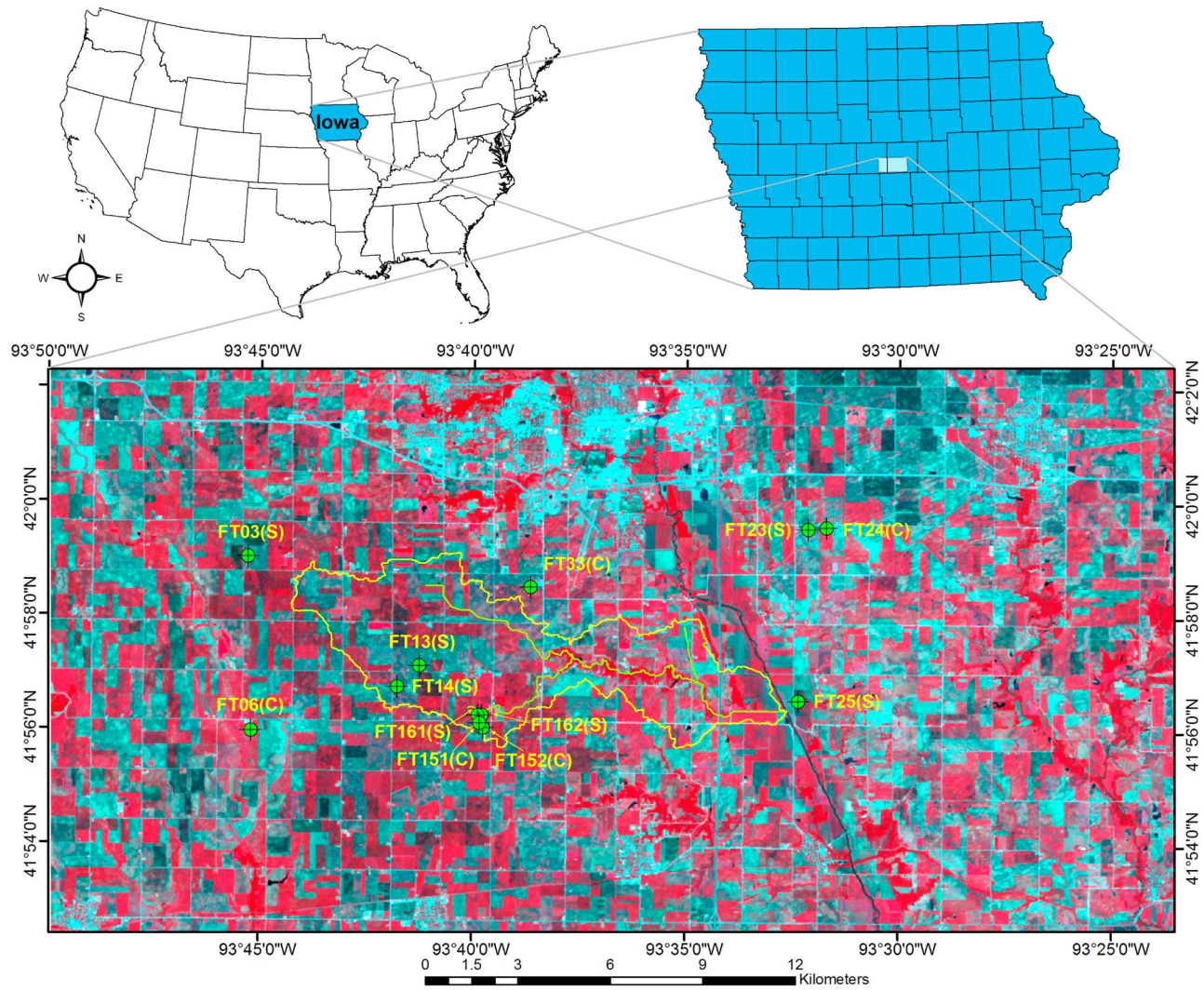


**Figure 2.** Location and the false-color composite of Landsat TM imagery acquired on 23 June 2002 of the SMACEX study site at Ames in central Iowa. The Walnut Creek watershed is delineated in yellow, and the main Walnut Creek and its branch are shown in olive. The METFLUX network, comprising 12 field sites, is shown in numbered green circles nested with cross wires. C denotes corn and S denotes soybean for crop types at EC towers.

[28] Three scenarios of the combinations of limiting edges for each domain were formulated. Scenario 1 represents the triangle model (equation (3)) with observed warm and cold edges derived from the NDVI- $T_{\text{rad}}$  space. Scenario 2 represents the triangle model (equation (3)) with the observed warm edge and the theoretical cold edge (i.e., areal average air temperature,  $T_m$ ). Taking  $T_m$  as the cold edge was motivated primarily by obviating the difficulty of demarcating cold edges from the NDVI- $T_{\text{rad}}$  space owing to relatively scattered points over low  $T_{\text{rad}}$  areas. Scenario 3 represents the trapezoid model (equation (13)) combined with the theoretical limiting edges shown in section 2.2.

[29] It is emphasized that scenarios 1 and 2 would result in varying observed limiting edges for different domains being studied. The cold edge of scenario 2 remains invariant owing to the use of  $T_m$ . Scenario 3 comprises theoretical limiting

edges specific for domain 1, which do not vary with the domain size.

#### 4.2. Variation in Limiting Edges With Domain Size

[30] Figures 4 and 5 illustrate scatterplots of NDVI and  $T_{\text{rad}}$  for four domains and relevant observed and theoretical limiting edges under three scenarios on days of year 174 and 182, respectively. Table 1 provides regression coefficients of the observed limiting edges for both days. It is apparent that the upper boundaries of these scatterplots at different domain scales tend to be relatively sharp; however, the lower boundaries seem to be poorly demarcated owing to many scattered points over areas with low NDVI and  $T_{\text{rad}}$  values, which may result mostly from clouds and standing water. The warm edge is therefore better defined than the cold edge. The poor demarcation of the cold edge is particularly exacerbated for domain 4 for both days. It could be

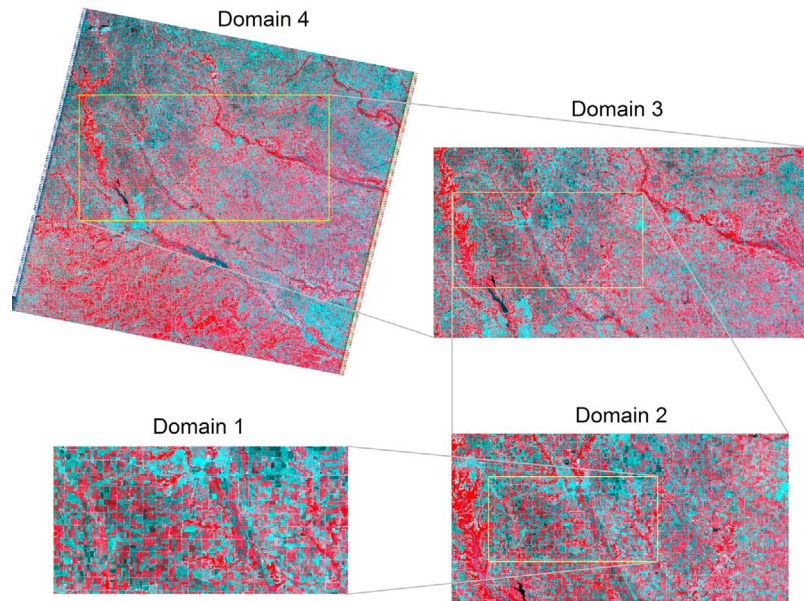


**Figure 3.** False-color composite of Landsat TM imagery acquired on 23 June 2002 covering the SMACEX site (domain 1), progressively enlarged domains 2 and 3, and the entire scene of the Landsat TM imagery (domain 4).

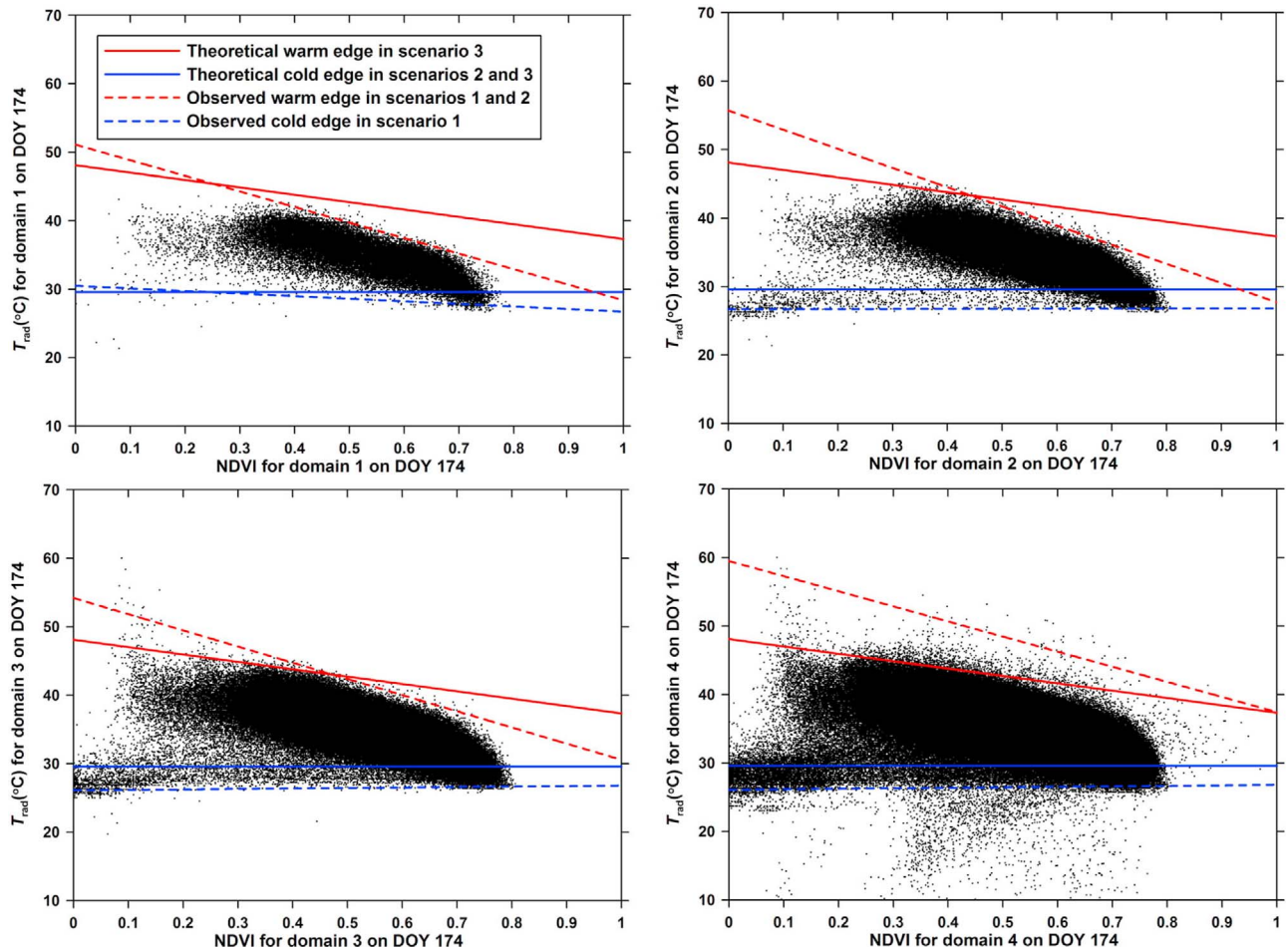


**Figure 4.** Scatterplots of NDVI and  $T_{rad}$  derived from Landsat TM imagery for four domains with relevant observed and theoretical limiting edges on DOY 174.

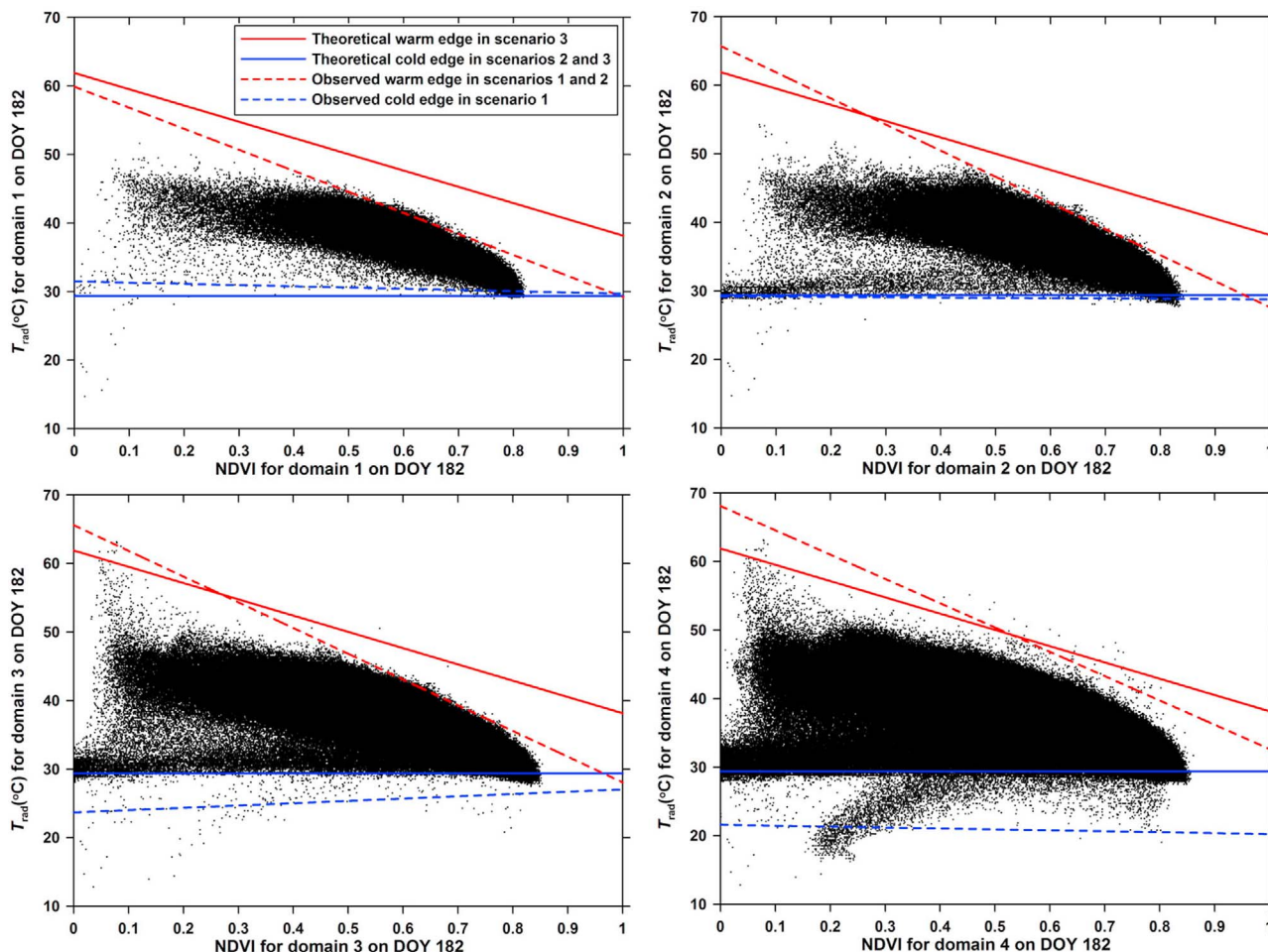


**Figure 5.** Scatterplots of NDVI and  $T_{rad}$  derived from Landsat ETM<sup>+</sup> imagery for four domains with relevant observed and theoretical limiting edges on DOY 182.

concluded that with an enlarging domain where a triangle model is applied, the likelihood of effectively or automatically delineating the cold edge decreases, especially for high-spatial-resolution imagery.

[31] In fact, many studies pertaining to triangle models utilized moderate- or low-spatial-resolution data (e.g., MODIS, NOAA-AVHRR, or MSG-SEVIRI imagery for a given study site) [Batra *et al.*, 2006; Stisen *et al.*, 2008; Tang *et al.*, 2010; Venturini *et al.*, 2004; Wang *et al.*, 2006], which may have circumvented the complexity arising from the use of high-spatial-resolution imagery; for example, Landsat TM/ETM<sup>+</sup>. The difficulty of demarcating the cold edge directly from the NDVI- $T_{rad}$  space results primarily from extraneous effects of  $T_{rad}$  retrievals for sloping terrain, shading, standing water, and clouds [Carlson, 2007; Gillies *et al.*, 1997]. This is also the reason why  $T_m$  was taken as the cold edge in scenarios 2 and 3 to circumvent uncertainties in the derivation of the cold edge.

[32] Furthermore, there are two key assumptions involved in triangle models.

[33] 1. Application of triangle models entails the existence of a range of soil moisture conditions, particularly covering extreme dry and wet surfaces for a full range of NDVI/ $f_c$  classes in a scene [Jiang and Islam, 1999, 2001; Sandholt

*et al.*, 2002; Stisen *et al.*, 2008]. This assumption often corresponds to a relatively large area of interest.

[34] 2. Differences in EF across a scene result mostly from differences in soil moisture conditions, instead of atmospheric conditions (e.g.,  $R_n$  and  $T_a$ ) and surface properties (e.g.,  $\alpha$ ) [Jiang and Islam, 2001; Stisen *et al.*, 2008]. The second assumption intrinsically constrains the extent of satellite images, which seems to be opposite to the first assumption. In practical applications, it would be really difficult to demarcate the extent of satellite images which can appropriately meet these assumptions. In central Iowa

**Table 1.** Regression Coefficients of Observed Limiting Edges Derived From Landsat TM/ETM<sup>+</sup> Imagery for Four Domains Around the SMACEX Site on Days of Year 174 and 182 in 2002

Domain	Warm Edge				Cold Edge			
	Slope		Intercept		Slope		Intercept	
	174	182	174	182	174	182	174	182
1	-22.71	-30.71	51.1	59.9	-3.77	-1.80	30.5	31.5
2	-27.97	-38.09	55.7	65.7	0.12	-0.42	26.7	29.2
3	-23.64	-37.53	54.2	65.6	0.70	3.35	26.1	23.7
4	-22.06	-35.45	59.5	68.1	0.70	1.35	26.1	21.6

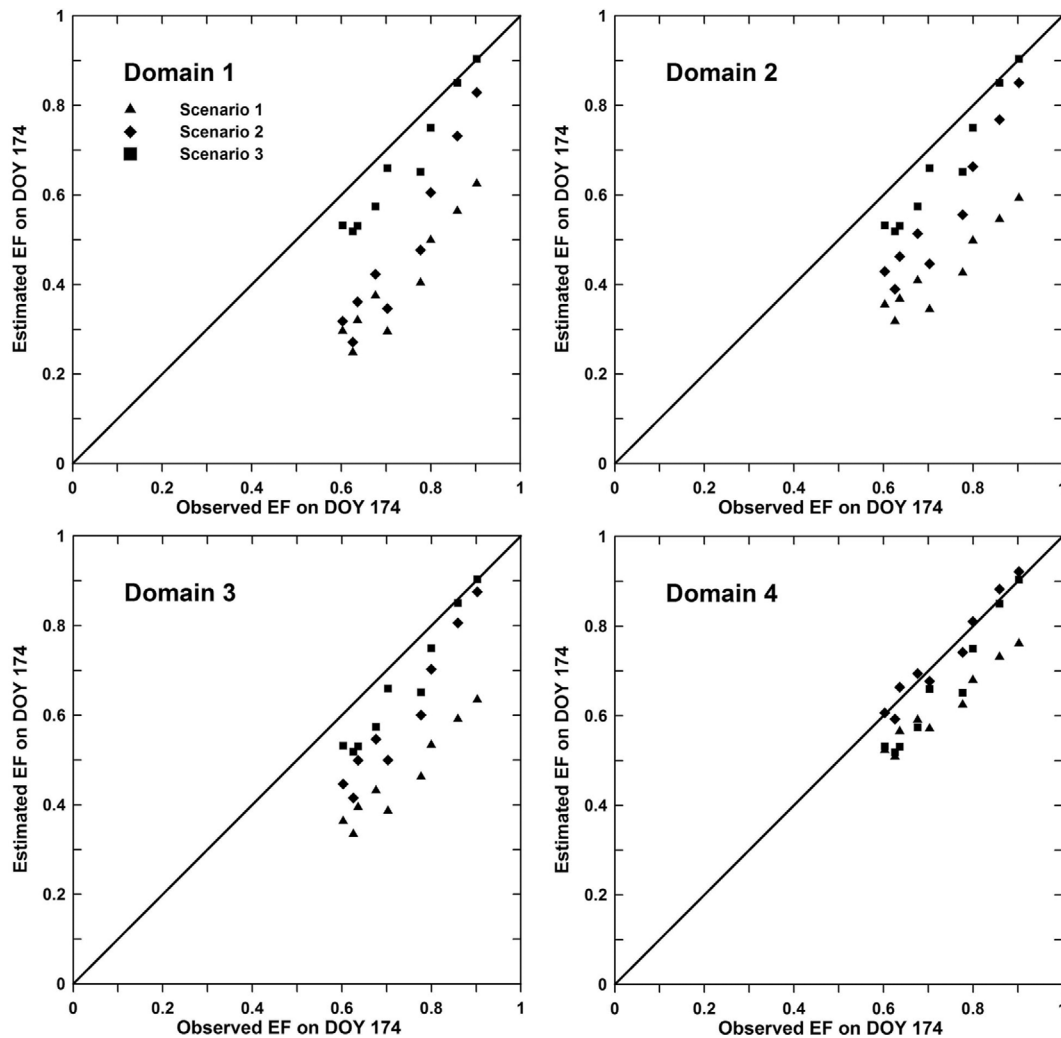


**Figure 6.** Comparison of EF estimates from triangle models and corresponding flux tower-based measurements for four domains on DOY 174 under three scenarios.

characterized primarily by agricultural crops, increasing the extent of modeling domain would not deviate greatly from the second assumption. However, for a general case, increasing the domain size would increase the heterogeneity in the land surface (e.g., encompassing more diverse land cover types), and consequently result in variations in the boundary conditions of triangle models. The overall triangle of the  $\text{NDVI}/f_c\text{-}T_{\text{rad}}$  space can then comprise mixed triangles, which needs to be decoupled for further analysis of EF and ET, but has not received much attention from the operational ET estimation community. Some studies applied triangle approaches to continental scales and paid less attention to the assumptions and applicability of those approaches [e.g., *Nishida et al.*, 2003a, 2003b; *Sun et al.*, 2009].

[35] Observed cold edge for domain 3 on DOY 174 was substituted for the observed cold edge for domain 4 as many scattered points over the lower boundary (probably represent cloud or standing water) resulted in failure to automatically demarcate the cold edge in domain 4.

#### 4.3. Variation in EF Estimates With Domain Size

[36] EF for the four study domains on days of year 174 and 182 under scenarios 1 and 2 was calculated using equation (3). EF on the two days under scenario 3 was calculated using equation (13). These EF estimates were averaged over the estimated upwind source area/footprint for each flux tower using the approach proposed by *Li et al.* [2008], and then compared with EF measurements (latent heat flux over the sum of latent heat and sensible heat fluxes) at each EC tower. Figures 6 and 7 give EF estimates and corresponding measurements for four domains under three scenarios on days of year 174 and 182, respectively. Figure 8 and Table 2 illustrate variations in the discrepancies between estimates and measurements with domain size. Results indicate that on DOY 174, the triangle model under scenarios 1 and 2 significantly underestimates EF within domains 1–3, suggesting a mean absolute percentage difference (MAPD) of 30–40% and 20–30% for scenarios 1 and 2, respectively. However, applying the triangle model to domain 4 under scenarios 1 and 2 appreciably improves accuracy, with an MAPD of 16% and 3.0%, respectively.

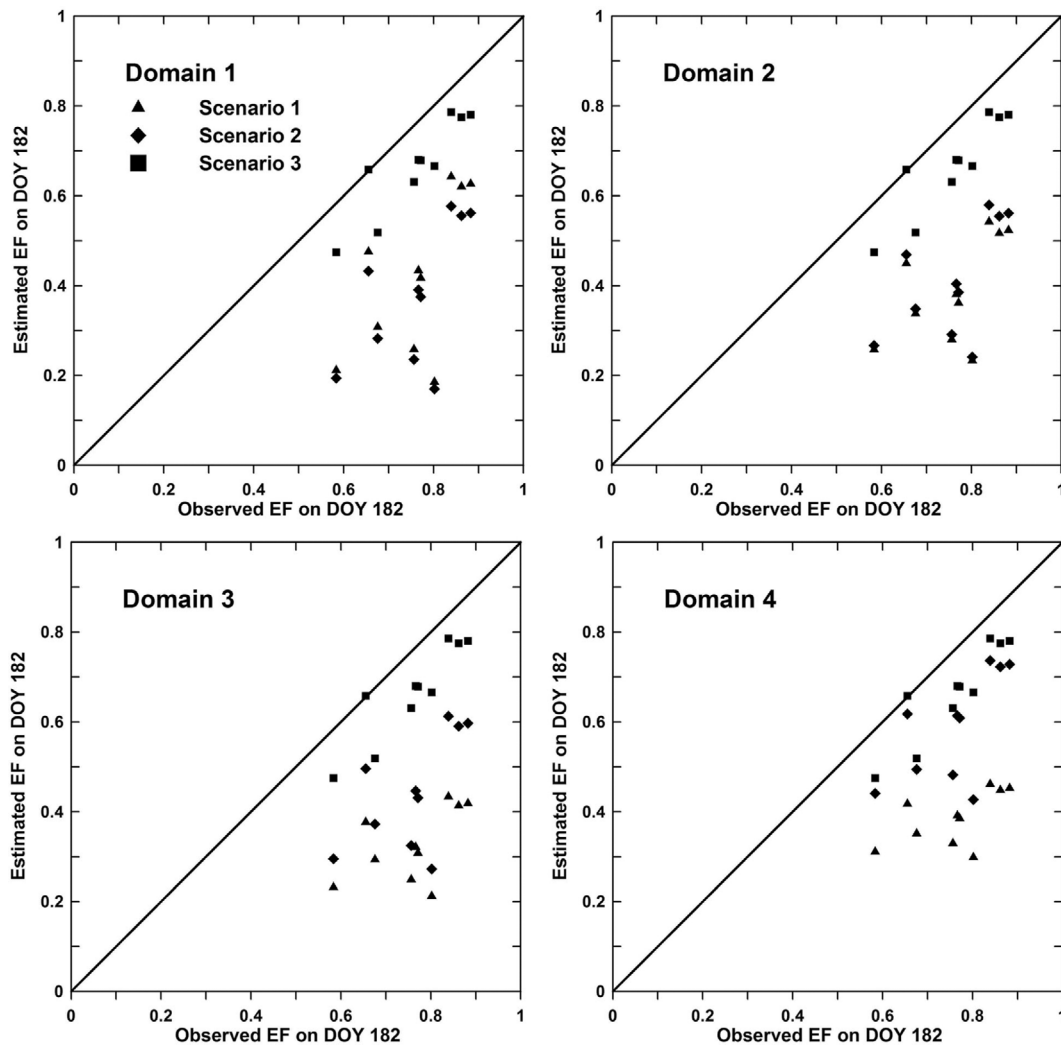


**Figure 7.** Comparison of EF estimates from triangle models and corresponding flux tower-based measurements for four domains on DOY 182 under three scenarios.

[37] In general scenario 2 results in more accurate EF estimates than scenario 1. In addition, with increasing domain sizes from 1 through 4, discrepancies between EF estimates and measurements consistently decrease (see DOY 174 in Figure 8). Variation in observed limiting edges with differing domains can explain these trends. First, for domain 1, EF from the triangle model in combination with the observed limiting edges was significantly underestimated, which could be ascribed to a significant downward shift of the observed warm edge compared with the theoretical upper limit, thereby resulting in the underestimated EF in terms of the monotonicity of equation (3). As the domain is enlarged, the observed warm edge tends to move upward (EF tends to increase) and the observed cold edge tends to move downward (EF tends to decrease) owing to a broader range of surface wetness conditions involved in the  $\text{NDVI}-T_{\text{rad}}$  space, with the magnitude of variation in the warm edge being larger than that of the cold edge. Therefore, underestimation of EF from the triangle model within domain 1 is mitigated to varying degrees as the domain is enlarged under both scenarios 1 and 2. In particular, scenario

2 leads to a more efficient improvement in the EF estimates owing to the use of a fixed cold edge for domain 1.

[38] For scenario 3, the trapezoid model within domain 1 results in an MAPD of 10% and 12% and a root mean square difference (RMSD) of 0.08 and 0.10 on days of year 174 and 182, respectively. These discrepancies demonstrate that the theoretical limiting edges can reproduce EF reasonably well, greatly improving the accuracy of the EF estimates compared with the triangle model in terms of an MAPD on the order of 30–50% and an RMSD on the order of 0.2–0.4. In particular, on DOY 182, the trapezoid model resulted in the highest accuracy in the four comparative domains than did the triangle model. Retrieval accuracy of EF on DOY 182 under scenarios 1 and 2 did not result in a marked improvement as the domain size increased, suggesting an MAPD on the order of 40–60% and 20–50% for scenarios 1 and 2, respectively. This may be as a result of a much higher theoretical warm edge compared with the observed edges. Despite within domain 4 which is most likely to include more dry surfaces/pixels, the scatterplot of  $\text{NDVI}-T_{\text{rad}}$  did not produce a reasonable warm edge and the EF estimates.

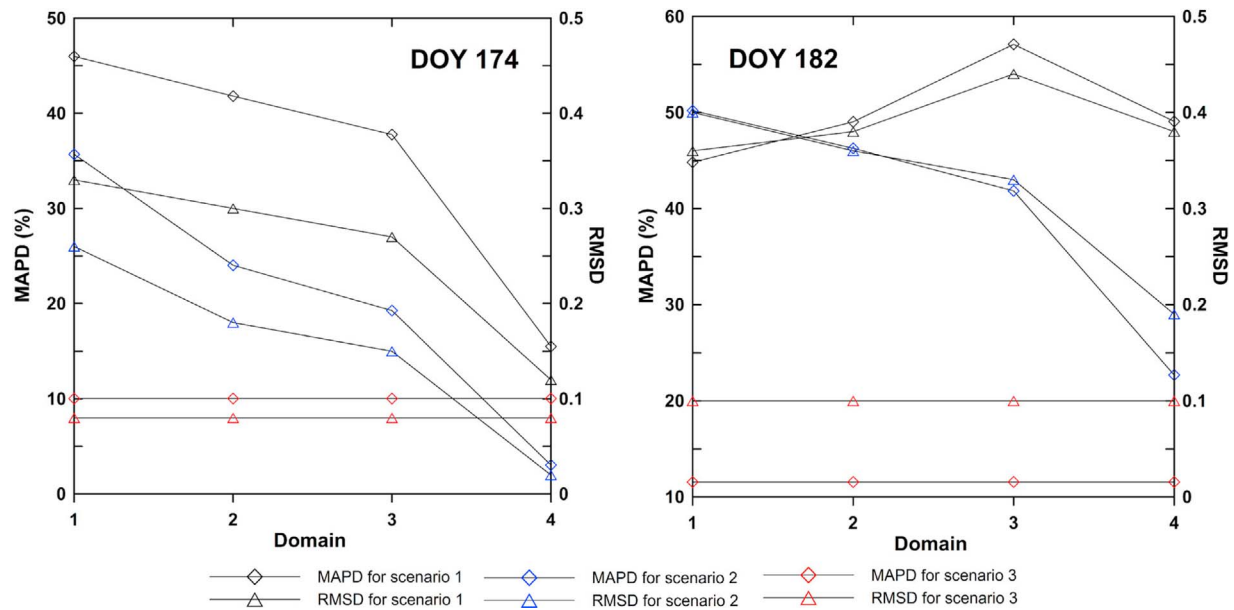


**Figure 8.** Variations in the mean absolute percentage difference (MAPD) and the root mean square deviation (RMSD) between the EF estimates from the triangle model under three scenarios and the measurements with the domain for days of year 174 and 182, respectively.

[39] Even though applying the triangle model to domain 4 on DOY 174 under scenario 2 showed greater accuracy than scenario 3, this is not the general case in practical applications because absolutely clear satellite images are not often available. More importantly, the user cannot precisely determine on which domain scale the theoretical limits can be approximated by the observed limiting edges by using the triangle model. This inadequacy is demonstrated by the case of DOY 182 that even though the entire scene of imagery was used to derive the limiting edges, the EF estimates from the triangle model were still unacceptable.

#### 4.4. Summary of Domain Dependence of the Triangle Model

[40] Applying the triangle model to varying domain sizes can result in varying observed limiting edges and consequently EF estimates. The triangle model can fail to generate EF with acceptable accuracy owing to the inability of the scatterplot of NDVI- $T_{\text{rad}}$  derived from a certain domain to include sufficient dry/wet surfaces. This inadequacy would be exacerbated if the theoretical limiting edges are beyond the range of soil wetness reflected by a scene of the satellite image.

[41] In general, the observed warm edge tends to move upward and the cold edge tends to move in the opposite direction as the domain is enlarged. The movement in the observed limiting edges can be ascribed to a broader range of soil wetness conditions as the domain is enlarged. To that end, retrieval accuracy of the EF estimates at a relatively small domain scale can be degraded or elevated as the domain is increased, depending on the magnitude of displacement of the observed limiting edges relative to the real physical limits. The trapezoid model in combination with the theoretical boundaries can remove in part the domain

dependence and ambiguity of EF retrievals intrinsic in triangle models.

## 5. Resolution Dependence of the Triangle Model

### 5.1. MODIS-Based NDVI- $T_{\text{rad}}$ Space

[42] Limiting edges for domains 1–4 from scatterplots of NDVI and  $T_{\text{rad}}$  from MODIS data products were derived. The MODIS-based scatterplots (Figure 9) were formed

**Table 2.** Discrepancies Between the Landsat TM/ETM<sup>+</sup>-Based EF Estimates and the Measurements<sup>a</sup>

Difference	DOY 174			DOY 182		
	Scenario 1	Scenario 2	Scenario 3	Scenario 1	Scenario 2	Scenario 3
	<i>Domain 1</i>					
RMSD	0.33	0.26	0.08	0.36	0.40	0.10
MAPD	45.98	35.69	10.03	44.81	50.19	11.55
Bias	-0.33	-0.25	-0.07	-0.34	-0.38	-0.09
	<i>Domain 2</i>					
RMSD	0.30	0.18	–	0.38	0.36	–
MAPD	41.81	24.02	–	49.02	46.26	–
Bias	-0.30	-0.17	–	-0.37	-0.35	–
	<i>Domain 3</i>					
RMSD	0.27	0.15	–	0.44	0.33	–
MAPD	37.76	19.26	–	57.08	41.83	–
Bias	-0.27	-0.13	–	-0.43	-0.32	–
	<i>Domain 4</i>					
RMSD	0.12	0.02	–	0.38	0.19	–
MAPD	15.50	3.04	–	49.07	22.68	–
Bias	-0.11	0.00	–	-0.37	-0.17	–

<sup>a</sup>Discrepancies include the following: root mean square difference (RMSD); mean absolute percentage difference (MAPD), and bias within four study domains at the SMACEX site on days of year 174 and 182 under three scenarios of configuration of limiting edges.

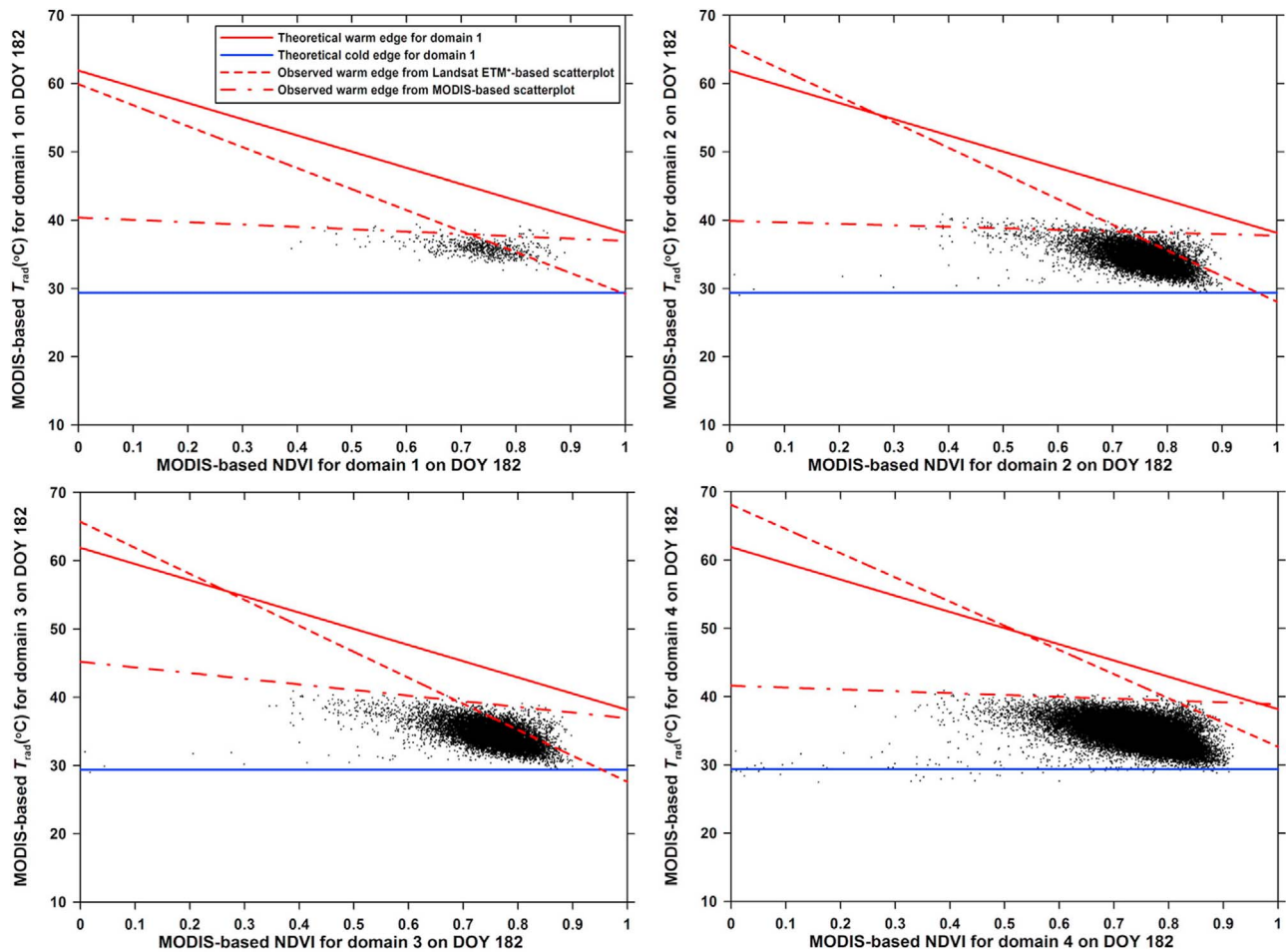


**Figure 9.** Scatterplots of 16 day composite NDVI (MOD13A2 on DOY 177) and  $T_{rad}$  (MOD11\_L2 on DOY 182) for four domains with relevant observed and theoretical limiting edges.

using MOD11\_L2 1 km-resolution LST products (including both LST and quality control images) and MOD13A2 1 km-resolution NDVI products (including both NDVI and quality control images). The MODIS-based scatterplots and the observed warm edges differ significantly from the Landsat ETM<sup>+</sup>-based counterparts for all study domains (referring to Figure 5). In general, the MODIS-based warm edges show gentler slopes and lower intercepts than the Landsat ETM<sup>+</sup>-based warm edges and the theoretical warm edge (see Figure 9 and Table 3). This is likely due to more prominent effects of the spatially integrated nature of the MODIS sensor compared with the Landsat ETM<sup>+</sup> sensor.

[43] The Landsat ETM<sup>+</sup> sensor is more capable of detecting subtle variations in  $T_{rad}$  and soil moisture conditions. The

1 km resolution of thermal infrared bands of the MODIS sensor does not seem to be able to discriminate variations in  $T_{rad}$  and soil moisture conditions at field scales (e.g., <500 m), resulting in a reduction in the range and standard deviation of  $T_{rad}$  and a generally downward displacement of the observed warm limits compared with the Landsat ETM<sup>+</sup>-based warm limits for each domain. The finding of the inability of the MODIS sensor to detect EF or LE flux at field scales reconfirms those of *Brunsell and Anderson* [2011] and *McCabe and Wood* [2006]. As such, moderate- or low-spatial-resolution sensors are not capable of capturing the complete picture of the NDVI- $T_{rad}$  space and therefore EF for relatively small study sites. Likewise, as the domain is enlarged, the observed warm edge tends to move upward

**Table 3.** Regression Coefficients of Observed Limiting Edges Derived From the Landsat ETM<sup>+</sup>

Domain	Warm Edge				Cold Edge			
	Slope		Intercept		Slope		Intercept	
	Landsat ETM <sup>+</sup>	MODIS						
1	-30.71	-3.44	59.9	40.4	-1.80	-6.68	31.5	39.7
2	-38.09	-2.15	65.7	39.9	-0.42	-6.76	29.2	37.5
3	-37.53	-8.27	65.6	45.2	3.35	-1.79	23.7	32.6
4	-35.45	-2.71	68.1	41.6	1.35	-0.41	21.6	29.4

<sup>a</sup>Image and MODIS-based  $T_{rad}$  and NDVI products for four domains around the SMACEX site on days of year 182 in 2002.

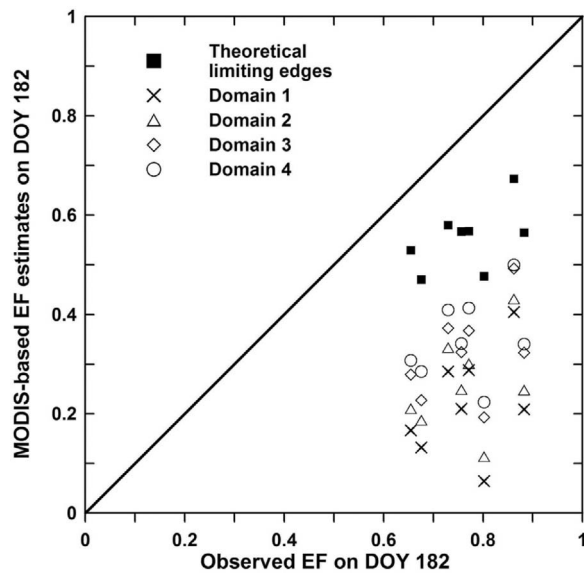


**Figure 10.** MODIS-based EF estimates and corresponding EF measurements for four domains on DOY 182. Solid squares represent EF estimates from the theoretical limiting warm edge and the cold edge of average air temperature of domain 1 ( $T_m$ ), and other symbols represent EF estimates from the observed warm edge and the cold edge formed by  $T_m$ .

owing to inclusion of a broader range of soil wetness. Therefore, the deviation of the MODIS-based observed warm edge from the theoretical warm edge is reduced to a certain degree.

## 5.2. MODIS-Based EF Estimates

[44] EF estimates from the triangle model in conjunction with the MODIS-based observed warm edge and the theoretical cold edge were compared with the corresponding EC tower measurements. EC towers 151, 152, and 162 were coincidentally located within the same pixel of the MODIS-based EF estimate. In this case, the EF estimate was compared with the averaged EF measurements within the 1 km-resolution pixel. The source areas/footprint of the EC towers are generally smaller than the pixel resolution of the MODIS-based EF estimates. This would introduce uncertainties in the comparison between the MODIS-based estimates and EC tower measurements. Evaluation of MODIS-based EF estimates still remains a big challenge in the operational ET estimation community. Given these limitations, the evaluation performed here is imperfect, but it may also provide valuable information associated with error propagation and performance of the triangle model.

[45] Results indicate that the MODIS-based EF estimates from the triangle model are degraded compared with those from the Landsat ETM<sup>+</sup> imagery, showing a bias on the order of  $-0.4$  to  $-0.5$ , an MAPD of 50–70%, and an RMSD of 0.4–0.5 for the four domains (see Figure 10 and Table 4). The EF was significantly underestimated. These differences are considerably larger than those from the Landsat ETM<sup>+</sup> data. Nonetheless, combining the trapezoid model with the MODIS data and the theoretical limiting edges results in an MAPD of 26% and an RMSD of 0.22, which are smallest in

**Table 4.** Discrepancies Between the MODIS-Based EF Estimates and the Measurements<sup>a</sup>

Domain	Difference	DOY 182	
		Scenario 1	Scenario 2
1	RMSD	0.54	0.22
	MAPD	69.06	25.53
	Bias	-0.53	-0.20
2	RMSD	0.50	—
	MAPD	63.32	—
	Bias	-0.48	—
3	RMSD	0.44	—
	MAPD	55.8	—
	Bias	-0.43	—
4	RMSD	0.41	—
	MAPD	51.48	—
	Bias	-0.40	—

<sup>a</sup>RMSD, MAPD, and bias within four study domains at the SMACEX site on DOY 182 under three scenarios of limiting edges.

the results from the triangle model for the four study domains. This demonstrates that use of theoretical limiting edges would constrain errors arising from resolution dependence of triangle models.

[46] Results suggest that as the domain size is increasing, MAPD and RMSD consistently decrease (see Figure 11 and Table 4). However, these differences are considerably larger than those of the Landsat ETM<sup>+</sup>-based estimates for each domain. Decreases in the MAPD and RMSD with increasing domain sizes are a consequence of a rising observed warm edge of the NDVI- $T_{rad}$  space as shown in Figure 9. However, even though applying the triangle model to a relatively large domain seems to result in improved EF outputs, the intrinsic assumption of similar radiation energy for the same NDVI/ $f_c$  class in the triangle model [Jiang and Islam, 2001]

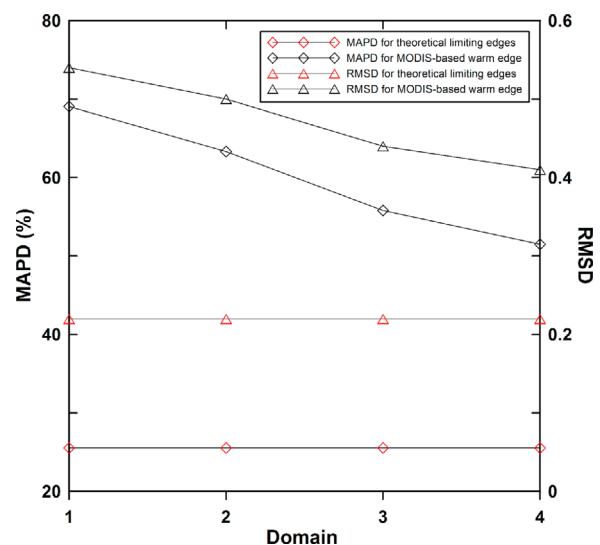


**Figure 11.** Variations in MAPD and RMSD between the MODIS-based EF estimates and the corresponding measurements with the domain on DOY 182.

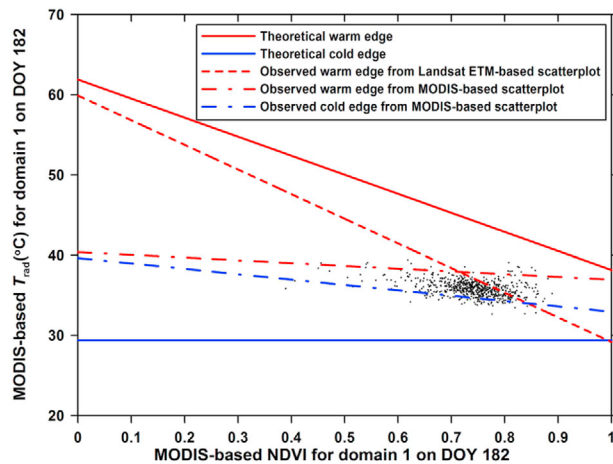


**Figure 12.** MODIS-based scatterplot of NDVI- $T_{\text{rad}}$  for domain 1 with observed and theoretical limiting edges on DOY 182.

would not be met. This would result in distorted EF distributions across the entire scene.

### 5.3. Coincidentally Reasonable EF Estimates From the Triangle Model

[47] As expounded above, the triangle model may suffer from domain and resolution dependencies. However, published studies associated with triangle models seem to report promising EF or ET results at a few towers. We suggest that there is a possibility that can coincidentally result in reasonable EF estimates from the triangle models. Figure 12 shows the MODIS-based scatterplot of NDVI and  $T_{\text{rad}}$  for domain 1 with both observed warm and cold edges. EF was simulated with the triangle model in combination with the observed limiting edges, showing an MAPD of 27% and an RMSD of 0.22. These discrepancies appear to be better than the results from the triangle model in combination with the theoretical cold edge for domain 1 ( $T_m$ ) and the observed warm edge showing an MAPD of 69% and an RMSD of 0.54. This is because even though the observed warm edge is significantly underestimated, the observed cold edge is significantly overestimated compared with the theoretical cold edge. The underestimation of EF owing to the downward shift of the warm edge and the overestimation of EF owing to the upward shift of the cold edge seem to offset each other, thereby resulting in seemingly reasonable results at a handful of EC towers in some cases.

[48] Reasonable EF results at a few EC towers do not necessarily mean generally reasonable EF retrievals throughout a scene. Given extreme cases, pixels on the observed warm and cold edges are mistakenly taken as hydrologic limits (i.e., for the warm edge with the largest water stress and for the cold edge EF = 1); and EF for pixels approaching the two observed limiting edges is overestimated (near the cold edge) or underestimated (near the warm edge). Only pixels with  $T_{\text{rad}}$  values around the spatial mean of  $T_{\text{rad}}$  would show reasonable results. If EC towers are not representatively distributed over a study site (e.g., across a range of soil wetness and in particular including extreme  $T_{\text{rad}}$  surfaces) or primarily concentrate in the middle portion of the  $T_{\text{rad}}$  distribution (i.e., moderate soil moisture

conditions), the resulting EF estimates would also show reasonable accuracy. Figure 13 provides the MODIS-based  $T_{\text{rad}}$  distribution for domain 1 and MODIS-based  $T_{\text{rad}}$  values at EC towers, showing that  $T_{\text{rad}}$  values at EC towers are essentially concentrated in the middle portion of the  $T_{\text{rad}}$  distribution. This means that the EF estimated from the observed limiting edges at these EC towers was probably coincidentally reasonable.

[49] This is the reason why a number of flux towers representatively distributed over a range of land covers and soil moisture conditions play a critical role in evaluation of satellite-based ET models. However, validation of satellite-based EF and ET estimates over large heterogeneous areas still remains a challenge for the operational ET estimation community owing to expensive instruments and uncertainties in scale effects and landscape heterogeneity [McCabe and Wood, 2006]. Our simulations and analyses have unraveled one possibility of coincidentally reasonable results produced at a few EC towers in the use of triangle models.

### 5.4. Summary of Resolution Dependence of the Triangle Model

[50] For a given study site, satellite images of differing spatial resolutions could result in largely different scatterplots of NDVI and  $T_{\text{rad}}$  and consequently disparate observed limiting edges. This would further result in different magnitudes and distributions of EF estimates. In general, use of moderate- or low-spatial-resolution satellite sensors would lose more information on subtle variations in  $T_{\text{rad}}$ , especially on hydrologic extremes compared with high-resolution images. The triangle model, therefore, suffers somewhat from resolution dependence. The trapezoid model in combination with the theoretical limiting edges can alleviate the resolution dependence to a certain degree. However, coincidentally reasonable EF estimates from the triangle models for pixels with  $T_{\text{rad}}$  values close to the spatial mean of  $T_{\text{rad}}$

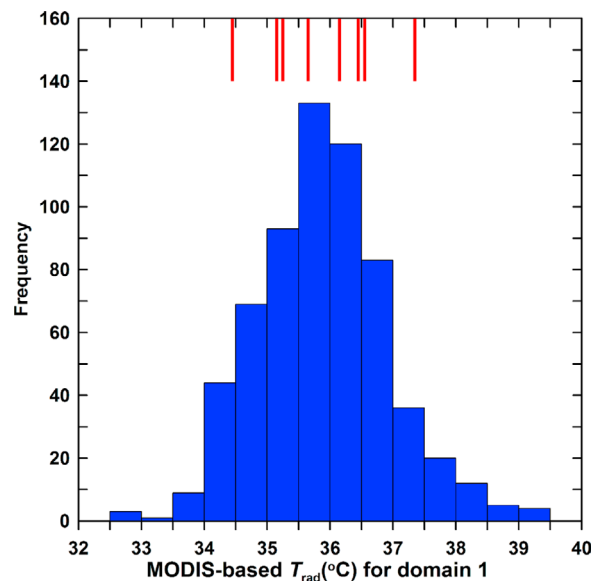


**Figure 13.** MODIS-based  $T_{\text{rad}}$  distribution (blue bars with a bin size of 0.5°C) for domain 1 and MODIS-based  $T_{\text{rad}}$  values at flux towers (red bars) on DOY 182.

across a scene would occur owing to overestimation of cold/warm edges and underestimation of warm/cold edges, whose effects on the resulting EF estimates could be offset.

## 6. Conclusions

[51] The major findings of the study are as follows:

[52] 1. As the domain size is increased, the observed warm edge tends to move upward (extreme high  $T_{\text{rad}}$  values increase) and the observed cold edge tends to move downward (extreme low  $T_{\text{rad}}$  values decrease). The resulting EF estimates from triangle models can therefore vary owing to the variation in limiting edges. The triangle models can be domain dependent.

[53] 2. Combining the triangle model with high-spatial-resolution images could be effective in EF estimation for relatively large study sites (e.g., on the order of  $>10^4$  km<sup>2</sup>). However, it fails to predict EF across relatively small study sites (e.g., on the order of  $<10^3$  km<sup>2</sup>). Degradation of predictions from the triangle model can be alleviated to a certain degree by selecting a larger domain size with a broader range of soil wetness conditions. This is, however, often constrained by the usable satellite image and its areal coverage, and the assumption of generally homogeneous radiation energy and atmospheric conditions.

[54] 3. Combining the triangle model with moderate- or low-spatial-resolution images could fail to discriminate extreme soil wetness conditions and consequently to detect EF, especially for relatively small study sites. The triangle models can be resolution dependent.

[55] 4. Analytically deriving limiting edges of the NDVI- $T_{\text{rad}}$  space can provide deterministic boundary conditions of the NDVI- $T_{\text{rad}}$  space and therefore reduce uncertainty and ambiguity in EF estimates. The theoretical warm edge can be derived by solving for temperatures of the driest bare surface and the fully vegetated surface with the largest water stress intrinsic in both radiation budget and energy balance equations. Area average air temperature can be taken as the theoretical cold edge.

[56] 5. The proposed trapezoid model using the theoretical limiting edges can constrain domain and resolution dependencies in EF estimation to a certain degree, making the NDVI/ $f_c$ - $T_{\text{rad}}$  approach applicable to relatively small areas.

[57] 6. Use of observed warm and cold edges in triangle models may result in coincidentally reasonable EF estimates for pixels with moderate  $T_{\text{rad}}$  values (e.g., around the spatial mean of  $T_{\text{rad}}$  across a scene) owing to underestimation (EF decreases)/overestimation (EF increase) of the warm edge and overestimation (EF increases)/underestimation (EF decreases) of the cold edge. The two effects can offset each other, but may distort EF distribution over surfaces/pixels approaching the observed limiting edges.

[58] **Acknowledgments.** We greatly thank the National Snow and Ice Data Center for providing the SMACEX data sets to validate the developed model. All people involved in the field campaign are gratefully acknowledged. We are grateful to three anonymous reviewers whose comments were helpful and constructive in improving the manuscript. This work was financially supported by the U.S. Geological Survey (project 2009TX334G) and the NASA program (NNH07ZDA001N).

## References

Allen, R. G., et al. (2007), Satellite-based energy balance for mapping evapotranspiration with internalized calibration (METRIC)—Model,

- J. Irrig. Drain. Eng.*, 133, 380–394, doi:10.1061/(ASCE)0733-9437(2007)133:4(380).
- Anderson, M. C., J. M. Norman, J. R. Mecikalski, J. A. Otkin, and W. P. Kustas (2007), A climatological study of evapotranspiration and moisture stress across the continental United States based on thermal remote sensing: 2. Surface moisture climatology, *J. Geophys. Res.*, 112, D11112, doi:10.1029/2006JD007507.
- Batra, N., et al. (2006), Estimation and comparison of evapotranspiration from MODIS and AVHRR sensors for clear sky days over the Southern Great Plains, *Remote Sens. Environ.*, 103, 1–15, doi:10.1016/j.rse.2006.02.019.
- Beven, K. J., and J. Fisher (1996), *Remote Sensing and Scaling in Hydrology*, John Wiley, Chichester, U. K.
- Brunsell, N. A., and M. C. Anderson (2011), Characterizing the multi-scale spatial structure of remotely sensed evapotranspiration with information theory, *Biogeosciences*, 8, 2269–2280, doi:10.5194/bg-8-2269-2011.
- Brunsell, N. A., et al. (2008), Assessing the multi-resolution information content of remotely sensed variables and elevation for evapotranspiration in a tall-grass prairie environment, *Remote Sens. Environ.*, 112, 2977–2987, doi:10.1016/j.rse.2008.02.002.
- Brutsaert, W. (1975), Derivable formula for long-wave radiation from clear skies, *Water Resour. Res.*, 11, 742–744, doi:10.1029/WR011i005p00742.
- Carlson, T. (2007), An overview of the “triangle method” for estimating surface evapotranspiration and soil moisture from satellite imagery, *Sensors*, 7, 1612–1629, doi:10.3390/s7081612.
- Carlson, T., et al. (1994), A method to make use of thermal infrared temperature and NDVI measurements to infer surface soil water content and fractional vegetation cover, *Remote Sens. Rev.*, 9, 161–173, doi:10.1080/02757259409532220.
- Carlson, T., et al. (1995), An interpretation of methodologies for indirect measurement of soil-water content, *Agric. For. Meteorol.*, 77, 191–205, doi:10.1016/0168-1923(95)02261-U.
- Choi, M., et al. (2009), An intercomparison of three remote sensing-based surface energy balance algorithms over a corn and soybean production region (Iowa, US) during SMACEX, *Agric. For. Meteorol.*, 149, 2082–2097, doi:10.1016/j.agrformet.2009.07.002.
- Garratt, J. R., and B. B. Hicks (1973), Momentum, heat and water-vapor transfer to and from natural and artificial surfaces, *Q. J. R. Meteorol. Soc.*, 99, 680–687, doi:10.1002/qj.49709942209.
- Gillies, R. R., and T. N. Carlson (1995), Thermal remote-sensing of surface soil-water content with partial vegetation cover for incorporation into climate models, *J. Appl. Meteorol.*, 34, 745–756, doi:10.1175/1520-0450(1995)034<0745:TRSOSS>2.0.CO;2.
- Gillies, R. R., et al. (1997), A verification of the “triangle” method for obtaining surface soil water content and energy fluxes from remote measurements of the Normalized Difference Vegetation Index (NDVI) and surface radiant temperature, *Int. J. Remote Sens.*, 18, 3145–3166, doi:10.1080/014311697217026.
- Jiang, L., and S. Islam (1999), A methodology for estimation of surface evapotranspiration over large areas using remote sensing observations, *Geophys. Res. Lett.*, 26, 2773–2776, doi:10.1029/1999GL006049.
- Jiang, L., and S. Islam (2001), Estimation of surface evaporation map over southern Great Plains using remote sensing data, *Water Resour. Res.*, 37, 329–340, doi:10.1029/2000WR900255.
- Jiang, L., and S. Islam (2003), An intercomparison of regional latent heat flux estimation using remote sensing data, *Int. J. Remote Sens.*, 24, 2221–2236, doi:10.1080/01431160210154821.
- Jiang, L., et al. (2009), A satellite-based daily actual evapotranspiration estimation algorithm over south Florida, *Global Planet. Change*, 67, 62–77, doi:10.1016/j.gloplacha.2008.12.008.
- Kalma, J. D., et al. (2008), Estimating land surface evaporation: A review of methods using remotely sensed surface temperature data, *Surv. Geophys.*, 29, 421–469, doi:10.1007/s10712-008-9037-z.
- Kondo, J. (1994), *Meteorology of Water Environment*, Asakura-shoten, Tokyo.
- Kustas, W. P., et al. (2005), The soil moisture-atmosphere coupling experiment (SMACEX): Background, hydrometeorological conditions, and preliminary findings, *J. Hydrometeorol.*, 6, 791–804, doi:10.1175/JHM456.1.
- Li, F. Q., et al. (2004), Deriving land surface temperature from Landsat 5 and 7 during SMEX02/SMACEX, *Remote Sens. Environ.*, 92, 521–534, doi:10.1016/j.rse.2004.02.018.
- Li, F. Q., et al. (2008), Effect of remote sensing spatial resolution on interpreting tower-based flux observations, *Remote Sens. Environ.*, 112, 337–349, doi:10.1016/j.rse.2006.11.032.
- Long, D., and V. P. Singh (2012), A modified surface energy balance algorithm for land (M-SEBAL) based on a trapezoidal framework, *Water Resour. Res.*, 48, W02528, doi:10.1029/2011WR010607.

- Long, D., et al. (2011), How sensitive is SEBAL to changes in input variables, domain size and satellite sensor?, *J. Geophys. Res.*, *116*, D21107, doi:10.1029/2011JD016542.
- McCabe, M. F., and E. F. Wood (2006), Scale influences on the remote estimation of evapotranspiration using multiple satellite sensors, *Remote Sens. Environ.*, *105*, 271–285, doi:10.1016/j.rse.2006.07.006.
- McVicar, T. R., and D. L. B. Jupp (2002), Using covariates to spatially interpolate moisture availability in the Murray-Darling Basin—A novel use of remotely sensed data, *Remote Sens. Environ.*, *79*, 199–212, doi:10.1016/S0034-4257(01)00273-5.
- Moran, M. S., et al. (1994), Estimating crop water-deficit using the relation between surface-air temperature and spectral vegetation index, *Remote Sens. Environ.*, *49*, 246–263, doi:10.1016/0034-4257(94)90020-5.
- Nemani, R., et al. (1993), Developing satellite-derived estimates of surface moisture status, *J. Appl. Meteorol.*, *32*, 548–557, doi:10.1175/1520-0450(1993)032<0548:DSDEOS>2.0.CO;2.
- Nishida, K., et al. (2003a), Development of an evapotranspiration index from aqua/MODIS for monitoring surface moisture status, *IEEE Trans. Geosci. Remote Sens.*, *41*, 493–501, doi:10.1109/TGRS.2003.811744.
- Nishida, K., R. R. Nemani, S. W. Running, and J. M. Glassy (2003b), An operational remote sensing algorithm of land surface evaporation, *J. Geophys. Res.*, *108*(D9), 4270, doi:10.1029/2002JD002062.
- Price, J. C. (1990), Using spatial context in satellite data to infer regional scale evapotranspiration, *IEEE Trans. Geosci. Remote Sens.*, *28*, 940–948, doi:10.1109/36.58983.
- Prueger, J. H., et al. (2005), Tower and aircraft eddy covariance measurements of water vapor, energy, and carbon dioxide fluxes during SMACEX, *J. Hydrometeorol.*, *6*, 954–960, doi:10.1175/JHM457.1.
- Sandholt, I., et al. (2002), A simple interpretation of the surface temperature/vegetation index space for assessment of surface moisture status, *Remote Sens. Environ.*, *79*, 213–224, doi:10.1016/S0034-4257(01)00274-7.
- Stisen, S., et al. (2008), Combining the triangle method with thermal inertia to estimate regional evapotranspiration—Applied to MSG-SEVIRI data in the Senegal River basin, *Remote Sens. Environ.*, *112*, 1242–1255, doi:10.1016/j.rse.2007.08.013.
- Sun, Z. G., et al. (2009), Development of a Simple Remote Sensing EvapoTranspiration model (Sim-ReSET): Algorithm and model test, *J. Hydrol.*, *376*, 476–485, doi:10.1016/j.jhydrol.2009.07.054.
- Tang, R. L., et al. (2010), An application of the Ts-VI triangle method with enhanced edges determination for evapotranspiration estimation from MODIS data in arid and semi-arid regions: Implementation and validation, *Remote Sens. Environ.*, *114*, 540–551, doi:10.1016/j.rse.2009.10.012.
- Tasumi, M. (2003), *Progress in Operational Estimation of Regional Evapotranspiration Using Satellite Imagery*, Univ. of Idaho, Moscow.
- Venturini, V., et al. (2004), Comparison of evaporative fractions estimated from AVHRR and MODIS sensors over south Florida, *Remote Sens. Environ.*, *93*, 77–86, doi:10.1016/j.rse.2004.06.020.
- Wang, K. C., et al. (2006), Estimation of evaporative fraction from a combination of day and night land surface temperatures and NDVI: A new method to determine the Priestley-Taylor parameter, *Remote Sens. Environ.*, *102*, 293–305, doi:10.1016/j.rse.2006.02.007.

D. Long and V. P. Singh, Department of Biological and Agricultural Engineering, Texas A&M University, College Station, TX 77843-2117, USA. (di.long@beg.utexas.edu)

B. R. Scanlon, Bureau of Economic Geology, Jackson School of Geosciences, University of Texas at Austin, 10100 Burnet Rd., Austin, TX 78758, USA.